Heat transfer in pyroclastic density current-ice interactions: insights from experimental and numerical simulations

Amelia. B. Vale[1], Luke. T. Jenkins[1], Jeremy. C. Phillips[1], Alison. C. Rust[1], Andrew. J. Hogg[2], Geoff. Kilgour[3], Anya. Seward [3]

[1]School of Earth Sciences, University of Bristol, Bristol, BS8 1RJ, United Kingdom
[2]School of Mathematics, University of Bristol, Bristol, BS8 1UG, United Kingdom
[3]GNS Science, 114 Karetoto Road, RD4, Taupō 3384, New Zealand

Key Points:

- We use experiments and modelling to investigate heat transfer from hot granular media to ice as an analogue to pyroclast-ice interactions.
- A systematic increase in melt and steam generation exists with increasing particle layer thickness and temperature.
- From our model we can derive meltwater source flux hydrographs, which show similarities with rainfall-driven lahar source hydrographs.

Corresponding author: Jeremy Phillips, J.C.Phillips@bristol.ac.uk

Abstract

Stratovolcanoes are common globally, with high altitude summit regions that are often glacier-clad and intersect the seasonal and perennial snow line. Explosive eruptions from stratovolcanoes can generate pyroclastic density currents (PDCs). When PDCs are emplaced onto and propagate over glacierised substrates, melt and steam are generated and incorporated into the flow, which can cause a transformation from hot, dry granular flow, to a water-saturated, sediment-laden flow, termed a lahar. Both PDCs and ice-melt lahars are highly hazardous due to their high energy during flow and long runout distances. Knowledge of the physics that underpin these interactions and the transformation to ice-melt lahar is extremely limited, preventing accurate descriptions within hazard models. To physically constrain the thermal interactions we conduct static melting experiments, where a hot granular layer was emplaced onto an ice substrate. The rate of heat transfer through the particle layer, melt and steam generation were quantified. Experiments revealed systematic increases in melt and steam with increasing particle layer thicknesses and temperatures. We also present a one-dimensional numerical model for heat transfer, calibrated against experiment data, capable of accurately predicting temperature and associated melting. Furthermore, we present similarity solutions for early-time melting which are used to benchmark our numerical scheme, and to provide rapid estimates for meltwater flux hydrographs. These data are vital for predicting melt volume and incorporation into PDCs required to facilitate the transformation to and evolution of ice-melt lahars.

Plain Language Summary

When volcanoes explosively erupt they may produce avalanches of hot, dry volcanic ash. When these volcanic avalanches occur on snow and glacier-covered volcanoes, they produce steam and melt, that can mix with the volcanic avalanche, transforming it to a cool, wet volcanic mudflow. Both volcanic avalanches and mudflows are extremely destructive and dangerous due to their high speeds and long flow paths. Historically, these flows have resulted in many fatalities and extensive building and infrastructure damage. We investigate the conditions under which transformation from volcanic avalanches to mudflows can occur. We use small-scale laboratory experiments to measure the transfer of heat, steam and melt generation when a hot ash layer is emplaced onto an underlying ice layer. We also present a numerical model to describe this heat transfer at large-scales, like in natural volcanic settings. This can be used to estimate the amount of melt required to cause this transformation from volcanic avalanche to mudflow. This can help us predict the destructiveness of these interactive events, and help us convey the hazard to stakeholders, and populations living in regions affected by volcano-ice interactions.

1 Introduction

Pyroclastic density currents (PDCs) are multiphase gravity currents composed of hot particles and gas that are generated by the gravitational collapse of an eruption column or lava dome (Druitt, 1998; Sulpizio et al., 2014; Lube et al., 2015; Dellino et al., 2021). They are produced by explosive volcanism and are highly destructive due to their high speeds, ranging from around 10 to > 100 ms^{-1} (Yamamoto et al., 1993; Cole et al., 1998; Belousov et al., 2002; R. S. Sparks et al., 2002; Scharff et al., 2019), and temperatures, typically ranging between 100-700°C (Banks & Hoblitt, 1996; Belousov et al., 2002; Cole et al., 2002; Druitt et al., 2002). The intermingling of the solid particles and fluid (gas) phase to varying extents produces a continuum ranging from dilute (gas-dominated) to concentrated (particle-dominated) PDCs. The incorporation of water into a PDC, for example from a river or melting of ice and snow, can fundamentally affect the dynamics of the flow.

When PDCs propagate over and are emplaced onto snow or ice they mechanically and thermally scour the substrate (Pierson et al., 1990; Walder, 2000b; Thouret et al., 2007). Following emplacement, heat is rapidly transferred from the particle layer to the ice, generating steam and melt that can be incorporated into the flow, causing dynamic transformations in both flow mobility and character (Figure 1). Generation and escape of steam can fluidise the flow, enhancing its overall mobility (Roche et al., 2002; Rowley et al., 2014). Incorporation of meltwater can affect the friction and cohesion properties of the bulk particle layer and can transform the flow into an ice-melt lahar if sufficient melt is generated (Branney & Gilbert, 1995; Huggel et al., 2007; Ahmed et al., 2012; Walding et al., 2023).

PDC interactions with frozen substrates are difficult to study *in-situ* due to their unpredictable and hazardous nature and poor preservation potential due to the susceptibility of snow and ice to melt out of deposits, reworking them in the process (Breard et al., 2020). Few evidence-based field studies of PDC-ice interactions and subsequent lahar generation exist. For example, highly detailed investigations were conducted following the catastrophic 1985 eruption of Nevado del Ruiz. These studies provide constraints on i) total ice loss and melt volume (Thouret, 1990), and ii) PDC, tephra fall and lahar events and deposits (Naranjo et al., 1986; Pierson et al., 1990). Kilgour et al. (2010) also provides a detailed study following the 25 September 2007 eruption of Ruapehu, which generated small-volume lahars. These studies provide context for the geophysical scale modelling described in 4.2. Complimenting detailed field studies, experiments and theoretical modelling can offer additional insights into the microphysical interactions between PDCs and frozen substrates.

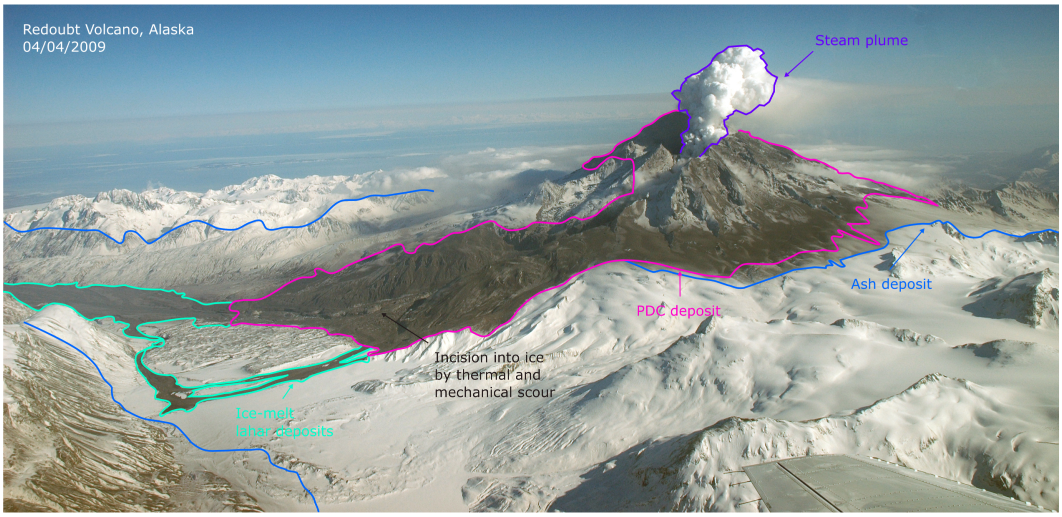

Figure 1. Redoubt volcano viewed from the northwest following the April 4, 2009 eruption. Annotations show volcanic processes and deposits. Incisions in the glaciated surface indicate thermal and mechanical scour by PDCs. Lahar deposits are observed downstream of the PDC deposits. Photo source: USGS (2009).

In order to comprehensively investigate the physics underpinning PDC-ice interactions, the thermal and mechanical effects must be isolated. The thermal effects can be studied by conducting experiments on a horizontal plane, where there is no relative shear motion or mechanical scour. In the natural system, the thermal interactions are most significant in the moments following PDC emplacement onto ice when the temperature gradient between the particle and ice is greatest, and steam and melt generation is most productive.

Few theoretical and experimental studies of hot particle-ice interactions exist offering insights into the heat transfer from particle to ice layers. Walder (2000a,b) developed a theory for pyroclast-snow interactions and thermally-driven slurry formation based on vertical thermal transfer between a porous hot particle layer and a snow substrate. Walder (2000a) presents the theory for monodisperse grain beds and Walder (2000b) presents the experimental results and extends the theory to polydisperse tephra. Experiments where heated sand was released onto shaved ice revealed a continuum of behaviours. Where no convective bubbling occurred within the sand layer, the particles melted into the snow as a wetting front rose upwards through the particle layer. In other cases rising vapour bubbles caused complete convective overturning of the particle layer by fluidisation, thermally scouring, and incorporating the snow, facilitating the transformation from a dry non-cohesive mass of particles into a slurry. The latter regimes were favoured by higher initial particle temperatures and smaller grain diameters. Cowlyn (2016) conducted complementary experiments to determine the amount of melting that could be generated by an individual pyroclast. These experiments provided numerical constraints for the rate of melt and steam production to inform predictive models of macroscopic PDC-ice interaction.

In this paper we focus on the thermal interactions between a layer of hot particles and ice. We extend the previous experimental work of Walder (2000b) and Cowlyn (2016) to include the interactions of volcanic and non-volcanic particles with ice across an expected thermal range for PDC-ice interactions. We report on the time evolution of temperature through the particle layer and the products generated by the interactions between hot particles and ice. We also present numerical simulations of this heat transfer, along with mathematical analysis at geophysical scales, highlighting the implications and importance of these simulations for natural PDC-ice interactions, and ice-melt lahar generation.

2 Materials and Methods

2.1 Experiments

We conducted a series of static melting experiments, where hot particles were poured onto a horizontal ice substrate to i) investigate heat transfer between the particle and ice layers, and ii) quantify melt and steam generation. These experiments were designed as an analogue to thermally-driven pyroclast-ice interactions. Our experiments used artificial and natural particle types to assess how particle composition and grain characteristics affected the rate of heat transfer. Our experiment data are freely available in an online repository (Vale et al., 2023).

2.1.1 Materials

Three particle types were used in the experiments: glass ballotini, crushed pumice (acquired from: Specialist Aggregates, product code: 7803), and an andesitic ash sample from Ruapehu Volcano. Glass ballotini have frequently been used in granular flow experiments because of their highly regular shape and packing structure, making them a good particle type for comparison purposes (Roche et al., 2004; Rowley et al., 2014). We selected the natural samples used in experiments to encompass a range of compositions, from felsic, vesicular volcanic glass (pumice) to more mafic and heterogeneous volcanic samples (Ruapehu). We constrained the grain characteristics for the three particle types through image acquisition and analysis techniques (Figure 2, Table 1).

Grain Characteristic	Glass Ballotini	Crushed Pumice	Ruapehu Ash
Grain size range (μm)	1000-1400	500-2000	500-2000
Sphericity	1	0.6-0.9	0.8-0.9
Density ρ (kgm^{-3})	2500	1080	2200
Vesicularity (%)	0	75-78	24-56
Thermal conductivity k ($Wm^{-1}K^{-1}$)	1.1-1.13	0.75	1.08-1.56

Table 1. Grain characteristics of the particle types used in static melting experiments.

We sieved the natural experiment samples to be within the 500-2000 µm grain size fractions, while Ballotini particles were pre-sorted into 1000-1400 µm sieve fractions. We used dynamic image analysis using a CAMSIZER X2 to determine particle grain size and shape distributions for all three particle types (Figure 2, Table 1) (Microtrac MRB, n.d.; Buckland et al., 2021). Particle sphericity is a measure of shape determined from the area and perimeter of an imaged particle, which has a maximum value of 1 for a perfect sphere (perfect circle in image, Figure 2). The ranges of

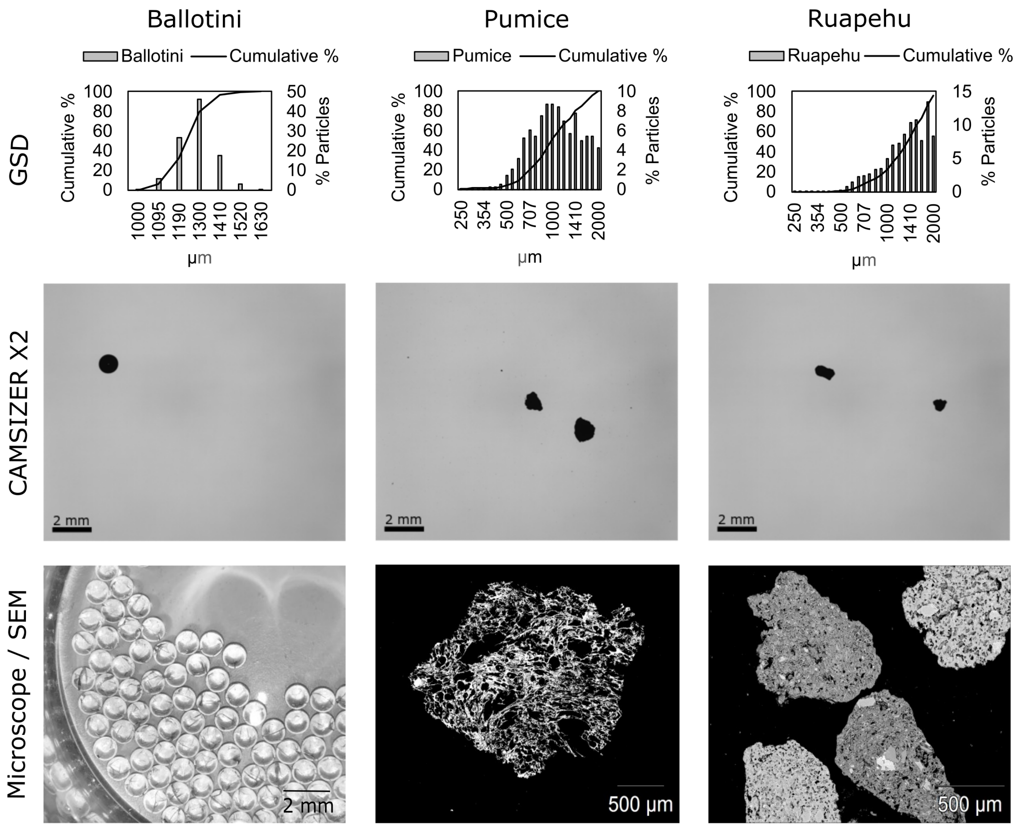

Figure 2. Grain size distributions (GSD) of experiment particle types, glass ballotini (left column), crushed pumice (central column), and Ruapehu ash / lapilli (right column), shown with Camsizer X2 imagery for shape analysis and Microscope/SEM imagery used for componentry and vesicularity analysis. SEM Voltage 20 kV, and working distance 22.4 mm.

sphericities varied for the three particle types. Ballotini particles are spherical, and regular in shape, with sphericities consistently close to 1. Ruapehu ash samples have sphericities ranging between 0.8-0.9. Pumice are the most variable in shape, with sphericities between 0.6-0.9.

We used a Hitachi S3500-N scanning electron microscope (SEM) operating in backscattered electron (BSE) mode at the University of Bristol to image and characterise Ruapehu ash and pumice samples particle componentry and vesicularity. The samples were mounted in epoxy resin, manually ground to grades PSI 240 to 1200, polished using a Buehler AutoMet 250 autopolisher to grades 9, 3 and 1 μm, and then carbon coated. Pumice samples were composed almost entirely of glass (> 95%), with few crystals present. Ruapehu ash samples were more varied in composition and texture, with the presence of microlites, phenocrysts and glass (Figure 2). We analysed SEM BSE images using *ImageJ*, an open-source, Java-based image processing software (Schneider et al., 2012). We manually edited the vesicles to remove trapped particle fragments to make the vesicle interiors the same intensity as the pure epoxy. We then thresholded the images to distinguish between the groundmass and vesicles. We calculated the percentage of vesiculated area in the image using the 'analyse particles' function within ImageJ, similar to Liu et al. (2017).

We measured particle density using a glass pycnometer, a measuring vessel with a precisely known volume. We initially filled the pycnometer with water, then we added a sample of one type of particles. We determined the volume of the particles by measuring the change in mass of the pycnometer with and without particles, and the volume of water displaced. We calculated density by dividing the mass of solids by the volume of solids, which is determined from the displacement of a fluid of known density from the pycnometer (Flint & Flint, 2002). Ballotini particles were the densest, and pumice particles were the least dense. This is consistent with particle vesicularity measurements, where ballotini particles had no vesicles, meanwhile pumice particles had a vesiculated area up to 78 %. The particle density determines the thermal mass of a material and also its efficacy at transferring heat. Typically, dense clasts will transfer heat to their surroundings more rapidly than porous clasts (Stroberg et al., 2010).

Bulk particle thermal properties in a water-saturated state were measured at room temperature using a Portable Electronic Divided Bar (PEDB, product code: Hot Dry Rocks HDR01), at GNS Science, Taupō, New Zealand. The PEDB determines a ratio between the thermal gradient across the sample and a known material. With this method, thermal conductivity measurements are accurate to within ± 3.5 % (A. M. Antriasian, 2009). Specific heat capacities were also determined by introducing a temperature perturbation and comparing the net thermal energy absorbed by the sample during thermal re-equilibration from one steady-state temperature to another (A. Antriasian & Beardsmore, 2014). Thermal conductivity measurements of experiment particle samples ranged from 0.75 to 1.56 $Wm^{-1}K^{-1}$, with pumice particles characterised by the lowest thermal conductivities, and Ruapehu ash particles the highest.

2.1.2 Experiment Configuration and Procedure

We initiated experiments by rapidly releasing hot particles onto a horizontal layer of ice contained within a cylindrical alumina beaker (75 mm diameter) whose initial temperature was approximately -20°C (Figure 3). The particle release lasted approximately 2 s, and over that time a layer of particles of uniform horizontal thickness was formed. We varied the mass of particles, and hence the particle layer thickness (5 - 45 mm). We also varied the initial temperature of particles over a range (200 - 700 °C) informed by PDC temperatures estimated by direct and proxy evidence (Banks & Hoblitt, 1996; Cole et al., 2002; Druitt et al., 2002; A. C. Scott & Glasspool, 2005; Lerner et al., 2019).

We recorded the evolution of temperature through the particle layer every second using eight ring-mounted type-K thermocouples at varying heights from the ice-particle interface (0 mm) up to 45 mm (surface of the thickest particle layer) (Figure 3). These thermocouples remained fixed in vertical and horizontal space for each experiment. After 10 minutes of particle-ice contact, we separated the particles from the ice and weighed the particles with the melt, dried them, and then reweighed them. We calculated melt as the mass difference between the wet particles (particles plus meltwater) and dry particles. We inferred the mass of steam generated as the difference between the mass loss of ice and total meltwater generated. From our experiments we yield a single measurement of the total amount of melt and steam produced in the 10 minutes after the particles first come into contact with the ice.

We conducted a limited set of experiments at lower temperatures (20 - 200 °C) and smaller particle depths (10 - 30 mm) using a larger, rectangular cross-section (330 x 230 mm) apparatus to confirm that the smaller-scale (75 mm diameter) static experiments were scalable to larger systems. Scaling between experiment configurations is presented in the Supplementary Material.

2.2 Numerical Simulations

We analyse a one-dimensional domain comprised of hot ash, of thickness d, overlying ice, with initial thickness H_0 (Figure 3). The coordinate system is upwards positive, with an origin defined such that $z = 0$ marks the initial position of the ash-ice interface. Melting of the ice will move the positions of the ash-ice interface $z = s(t)$, and air-ash interface $z = d + s(t)$.

In each solid phase, thermal diffusion is described by

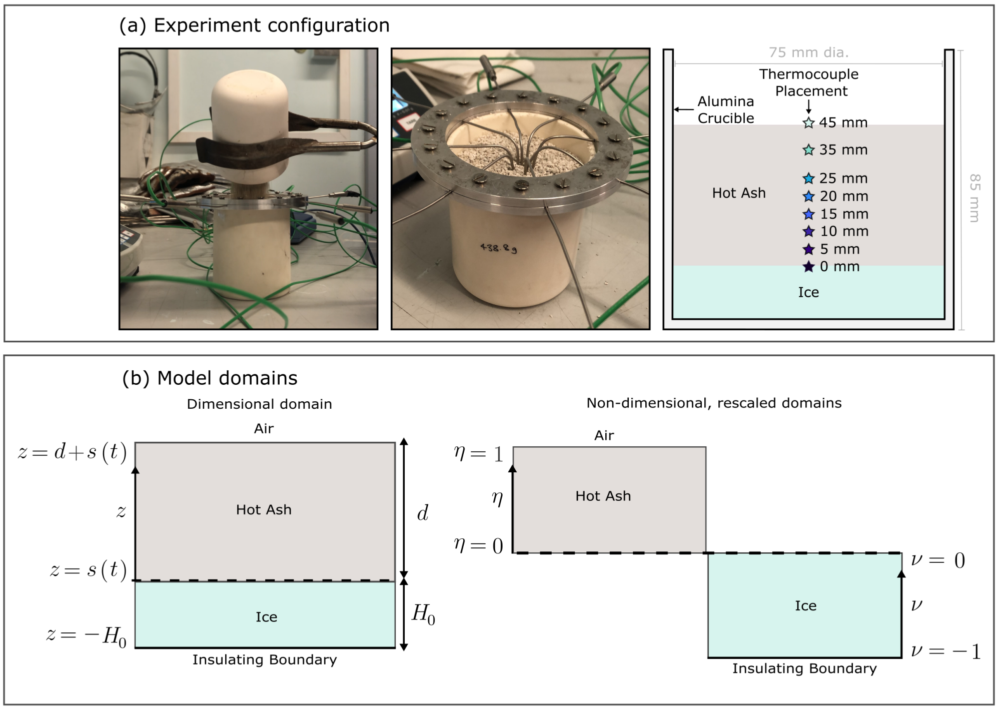

Figure 3. Experimental configuration and model domains. (a) Particles are poured through a thermocouple array onto a horizontal layer of ice. Temperature is recorded using a ring-mounted thermocouple array supporting eight type-k thermocouples set at different heights through the particle layer. Thermocouple heights are denoted by star markers. (b) Schematic diagrams of our numerical domains. For numerical convenience, we non-dimensionalise and rescale our dimensionless coordinate system (left) into separate subdomains (right) for each phase (see Appendix A).

$$\rho_j c_{p,j} \frac{\partial T}{\partial t} - \frac{\partial}{\partial z}\left(k_j \frac{\partial T}{\partial z}\right) = 0, \tag{1}$$

where $j = [A, I]$ denotes the solid phase for ash and ice respectively; ρ_j, $c_{p,j}$ and k_j are the density, specific heat capacity and thermal conductivity of the j^{th} solid phase respectively. For simplicity, we consider thermal transport in the solid phases only i.e., higher-order thermal effects associated with the imbibition of meltwater are neglected. In Section 4.1, we calibrate our model and demonstrate that this is a reasonable assumption.

During melting, conservation of energy requires that the latent heat of melting (L) is balanced by the difference in heat flux across the ash-ice interface:

$$\rho_I L \frac{\mathrm{ds}}{\mathrm{dt}} = k_I \frac{\partial T}{\partial z}\bigg|_{z=s^-} - k_A \frac{\partial T}{\partial z}\bigg|_{z=s^+}, \qquad \text{with} \quad T(z = s(t)) = T_m, \tag{2}$$

where T_m is the melting temperature of ice and $q = -k_j(\partial T/\partial z)|_{z=s}$ is the heat flux, given by Fourier's law, evaluated at the ash-ice interface. This equation—which is often referred to as the Stefan condition—is widely used in moving-boundary problems to describe the velocity of a phase-change interface (e.g., Meirmanov, 2011). Note that due to our sign convention, melting occurs when $\mathrm{ds}/\mathrm{dt} < 0$. Therefore, the cumulative melt at time t is given by $-(\rho_w/\rho_I)s(t)$, where ρ_w is the water density.

A Dirichlet condition is required to couple the ash and ice subdomains. The magnitude of the interface temperature must account for occurrence, or absence, of melting. Melting is an isothermal process; meaning that the interface temperature is pinned at the melting temperature when Equation (2) is negative. When melting terminates, the heat flux either side of the interface is continuous. Solving Equation (2) with $\mathrm{d}s/\mathrm{d}t = 0$ yields a Dirichlet condition for the interface temperature that is a weighted arithmetic mean of ash and ice temperatures either side of the interface.

At the top boundary, heat losses to the air are likely dominated by convection, which are approximated by equating the surface heat flux to a linear constitutive function that is proportional to the temperature difference at the surface:

$$-k_A \frac{\partial T}{\partial z} = c\,(T - T_{\mathrm{air}}), \qquad \text{at} \quad z = d + s(t), \tag{3}$$

where T_{air} is the ambient air temperature, and c is a dimensional parameter that control the strength of convective heat losses (e.g., Vollmer, 2009). It is assumed that the basal boundary is perfectly insulating:

$$\frac{\partial T}{\partial z} = 0, \qquad \text{at} \quad z = -H_0. \tag{4}$$

This is likely a reasonable assumption for most geophysical settings, where the heat capacity of ice greatly exceeds that of ash $(\rho_I c_I H_0)/(\rho_a c_A d) \gg 1$. This is confirmed in Section 4.1, where we demonstrate that our model calibration improves as d/H decreases. In all cases, a uniform initial temperature distribution in the ice $(T_I(t = 0, z))$ is assumed. When calibrating our model at the laboratory scale, we use an initial temperature distribution $(T_A(t = 0, z))$ that is determined experimentally (see Section 4.1). At geophysical-scales (Section 4.2), we assume for simplicity that $T_A(t = 0, z)$ is uniform.

2.2.1 Non-dimensionalisation and rescaling

To better understand the key controls of volcanically-induced ice melting, we reduce the number of parameters in our model by non-dimensionalising the governing equations and boundary conditions using rescaled variables

$$\tilde{z} = z/d, \quad \tilde{t} = t/\tau, \quad \tilde{T} = T/\vartheta, \quad \text{and} \quad \tilde{s} = s/d, \tag{5}$$

in combination with characteristic scales

$$\tau = \frac{d^2}{\alpha_A}, \quad \text{and} \quad \vartheta = \frac{\rho_I L}{\rho_A c_{p,A}}. \tag{6}$$

Note that the characteristic timescale is diffusive, whereas the characteristic temperature scale is a ratio between the volumetric latent heat of ice to the volumetric heat capacity of ash.

The remaining dimensionless parameters are

$$R_\alpha = \frac{k_I \rho_A c_{p,A}}{k_A \rho_I c_{p,I}} \equiv \frac{\alpha_I}{\alpha_A}, \tag{7a}$$

$$R_k = \frac{k_I}{k_A}, \tag{7b}$$

$$\mathrm{Nu} = \frac{cd}{k_A}, \tag{7c}$$

$$H = \frac{H_0}{d}, \tag{7d}$$

where α_j is the thermal diffusivity of the j^{th} phase. To avoid numerical complexities associated with solving diffusion in a shrinking (ice) domain, we transform our dimensionless coordinate system onto a fixed domain using a bilinear mapping (see Figure 3 and Appendix A). Dropping the tilde notation used above, the resulting remapped non-dimensional governing equations are:

$$\frac{\partial T}{\partial t} = \frac{\mathrm{ds}}{\mathrm{dt}}\frac{\partial T}{\partial \eta} + \frac{\partial^2 T}{\partial \eta^2}, \qquad \text{for} \quad 0 < \eta < 1, \tag{8a}$$

$$\frac{\partial T}{\partial t} = \left(\frac{1+\nu}{H+s}\right)\frac{\mathrm{ds}}{\mathrm{dt}}\frac{\partial T}{\partial \nu} + \frac{R_\alpha}{(H+s)^2}\frac{\partial^2 T}{\partial \nu^2}, \qquad \text{for} \quad -1 < \nu < 0, \tag{8b}$$

$$\frac{\mathrm{ds}}{\mathrm{dt}} = \frac{R_k}{H+s}\frac{\partial T}{\partial \nu}\bigg|_I - \frac{\partial T}{\partial \eta}\bigg|_A < 0, \qquad \text{with} \quad T(\eta = \nu = 0) = T_m \tag{8c}$$

$$\frac{\partial T}{\partial \eta} = -\mathrm{Nu}(T - T_{\mathrm{air}}), \qquad \text{at} \quad \eta = 1. \tag{8d}$$

Note that rescaling Equation (1) introduces advective terms to account for the motion of the ash-ice interface, such that thermal transport is now described by two coupled advection-diffusion equations with four principle parameters: R_α, which compares the strength of thermal diffusion (α_j) in the ice and ash; R_k compares the strength of thermal conduction in the solid phases; H compares the initial thicknesses of the solid phases; and the Nusselt number Nu is the ratio of convective to conductive heat transfer at the surface of the ash ($\eta = 1$).

We solve this coupled system of ordinary and partial differential equations using the method of lines (e.g., Schiesser, 2012). We use a standard first-order finite-volume scheme to discretise our remapped spatial domains; allowing for the resulting system of equations to be expressed as a series of coupled ordinary differential equations (ODEs), which are integrated in time using `MATLAB's` stiff ODE solver `ODE15s` (Shampine & Reichelt, 1997). We provide the ODE solver with the pattern of the Jacobian matrix. This significantly reduces the computation time by allowing the solver to only evaluate the Jacobian's non-sparse elements (e.g., Goudarzi et al., 2016). We validate our model in Section 4.2, where we demonstrate that our numerical scheme agrees with similarity solutions that describe early-time diffusive melting. We verify the convergence of our numerical scheme by exploring the effect of grid resolution on the melting end state $s_\infty \equiv s(t \to \infty)$ in the reference case used in Section 4.2. For our simulations, we use 2500 grid cells in each solid phase. At this resolution, simulations take ~9 seconds on a single `i7-6500U` processor, compared with a run time of ~65 seconds for simulations that do not utilise the Jacobian pattern. Further reducing the grid spacing results in variations to $|s_\infty|$ by less than 0.8%. Our numerical solver and associated plotting scripts are freely available in an online repository (Vale et al., 2023).

3 Experimental Results

3.1 Heat Transfer from Particle to Ice

We obtained the time evolution of temperature at set heights through the particle layer using eight type-K thermocouples. The thermocouples captured the initial spike in temperature following emplacement and the subsequent cooling of the particles as heat was transferred from the particle layer to the underlying ice and air above (Figure 4).

The peak particle temperatures recorded by the thermocouples rarely reached the furnace temperature where the particles were heated. This is related to cooling as particles are removed from the furnace, transported 1.5 m, and then poured c.10 cm into the ice container. Thicker particle layers and particles characterised by lower thermal conductivities retained more heat in transit and release and so attained higher peak temperatures. Peak temperatures were recorded by the thermocouples at different times for different particle types and temperatures. At higher peak temperatures the thermocouples took longer to equilibrate with the particles. Ballotini particles reached peak temperatures fastest, meanwhile pumice particles reached peak temperatures slowest. This results from the particle's thermal conductivity. In line with this, ballotini particles also reached thermal equilibrium fastest, and pumice the slowest. Within individual experiments the peak

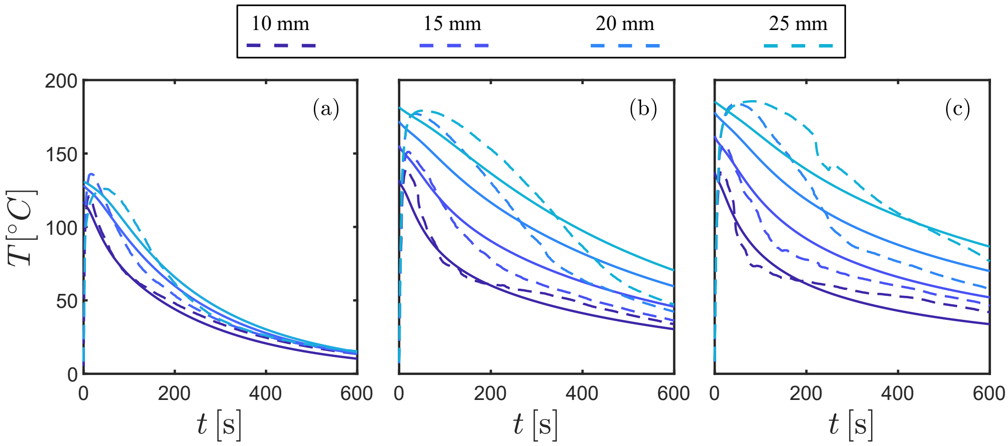

Figure 4. Thermal evolution for 200°C Ruapehu ash experiments and simulations for d = 20 (a), 34 (b), and 45 (c) mm respectively. Both simulated (solid) and experimental (dashed) curves correspond to thermocouples located at z = [10, 15, 20 and 25] mm above the ash-ice interface (dark-light blue).

temperatures obtained by thermocouples varied with position through the particle layer. Typically, the highest temperatures were recorded in the mid-particle region, with cooler peak temperatures recorded closer to the ice and the particle surface.

The temperature data recorded steam generation signals in two forms, i) as noise in the thermocouple data, and ii) as a period of stability around 100°C (see Supplementary Material). We used these signals to determine the duration and intensity of steam generation in experiments. We interpreted noise in the temperature data as sporadic generation and release of steam as melt came into contact with particles exceeding the minimum temperature required for steam generation. We interpreted stability around 100 °C as continuous boiling and generation of steam. Of the three particle types examined, pumice particles produced the least steam. This is supported by a general lack of noise or thermocouple stability around 100 °C in the temperature data. Ballotini and Ruapehu ash particles produced significant amounts of steam in some experiments. The experiment that produced the most steam, B_M250_T700 (34.81 g), generated steam for over 300 seconds, or half the total experiment duration, based on duration of the noise signal.

We observed stepped reductions in the particle temperature followed by stabilising of the temperature curves in some experiments (e.g., Figure 4c). These steps were initially recorded close to the particle-ice interface, but were subsequently recorded by sequentially higher thermocouples in the particle layer. We observed these stepped features across all particle types, most notably in experiments with greater particle thicknesses. These steps were identified as rising meltwater coming into contact with the thermocouples. We calculated the rate of movement of the meltwater front by dividing the distance between successive thermocouples by the time elapsed between successive steps in the temperature profiles. Where drops in the temperature profiles were not simultaneous due to steam escape, rates of meltwater front movement ranged between 0.04-0.59 mm/s. Where steam escaped through the particle layer these temperature profile steps were observed at multiple successive thermocouples simultaneously.

3.2 Melt and Steam

We observed a systematic increase in melt with increasing particle layer mass (therefore layer thickness) and temperature across all particle types (Figure 5). Pumice and Ruapehu ash melt masses show greater sensitivity than ballotini melt masses to increasing particle temperature. The melt data

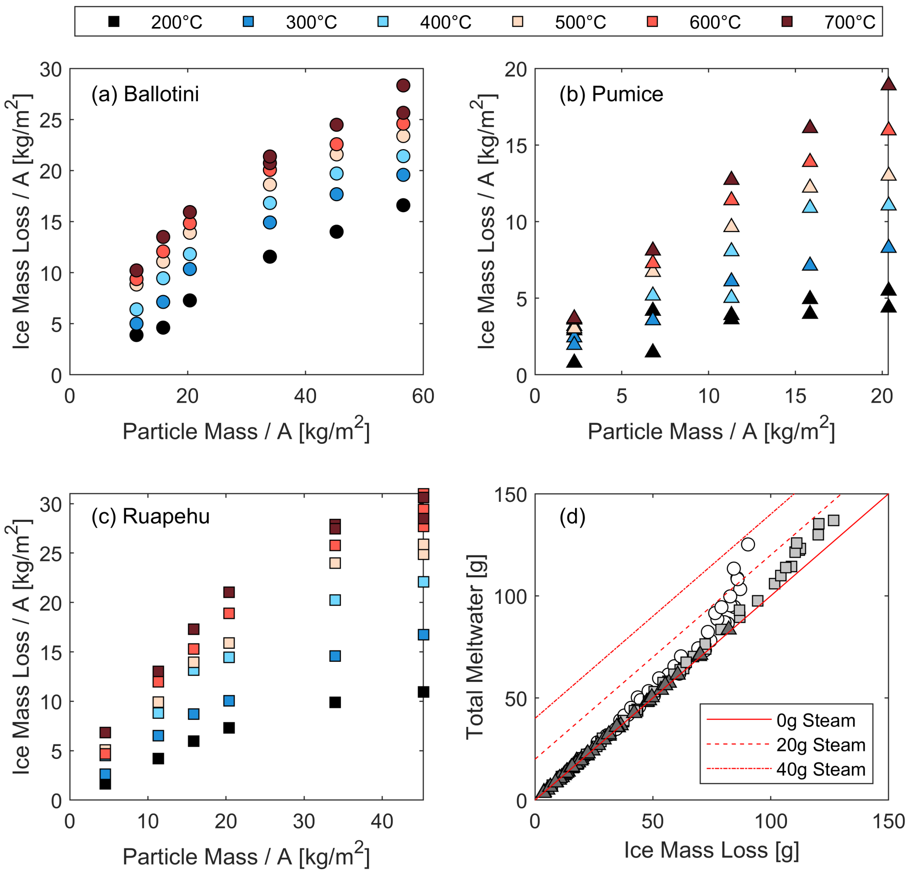

Figure 5. Panels (a-c) Ice Mass Loss as a function of the mass of heated particles of different initial temperatures. The ice and particle masses are normalised by their horizontal surface area in contact. Panel (d) Total Meltwater against Ice Mass Loss, where deviation from x = y is equal to steam. Particle types are denoted by symbol and correspond to the same symbol shapes as panels a-c.

also show a reduction in the rate of increase in melt with increasing particle layer thickness for all particle types.

Steam generation also systematically increased with particle mass and temperature for ballotini and Ruapehu ash particles, but steam generation was negligible for pumice (Figure 5d). Ballotini particles produced the most steam for any given layer thickness and were more sensitive to particle temperature than the other particle types. The differing sensitivities of particles to layer thickness and temperature in generating melt and steam are caused by variations in both bulk particle and individual grain characteristics, specifically grain shape, density, thermal mass, and thermal conductivity.

Melt was observed to be brought to the surface via three principal mechanisms, i) a vapour-bubble supported melt lens, ii) flash steam escape events, and iii) passive sinking of the particle layer into ponded melt at the ash-ice interface.

The generation and escape of steam through the upper particle layer also offered insights into the thermodynamics of particle-ice interactions. As expected, steam generation was most productive in the first seconds to minutes following emplacement, where the duration of steam production was dependent on the initial experiment conditions, with the hottest temperatures and thickest particle layers producing steam for the longest durations. Where steam was produced the particles could be fluidised for up to 10 seconds. Fluidisation of Ruapehu ash particles also resulted in the elutriation of fines from the particle layer in experiments, a phenomenon frequently reported in pyroclastic literature, for example Wilson (1980), Fisher (1995), and Kelfoun & Gueugneau (2022). In experiments steam escape via the surface could also be localised and temporally sporadic. The sporadic nature of this steam escape is likely caused by an upward-moving meltwater front coming into contact with dry particles that remain above a critical temperature. The escape of steam via the upper particle surface also brought melt to the surface with it, highlighting that steam escape encourages particle layer mixing and incorporation of melt.

The quantifications of melt and steam are in agreement with the temperature data, confirming that ballotini are the most efficient and pumice the least efficient at transferring heat from the particle layer (Figure 5). Efficient transfer of heat from the particle layer into the ice can be attributed to the high density and thermal mass, and regular packing structure of ballotini particles which enables efficient transport of melt and steam through the particle layer because the regularly-packed configuration is low permeability. Pumice particles were the least efficient due to their low density and thermal mass, and irregular packing structure. Ruapehu ash particles fall in between ballotini and pumice end members.

4 Modelling results

4.1 Model calibration

We calibrate our model using experiments with Ruapehu ash particles heated to 200°C. These experiments provide two sets of measurements that must be approximated by a well-calibrated model: (1) thermal evolution of the ash measured by internal thermocouples; (2) a single measurement of ice melting, recorded after 10 minutes. In addition to these experimental constraints, our model calibration is further aided by experimental measurements of the specific heat capacity and thermal conductivity of the ash. Moreover, the physical properties of ice are well constrained in the literature. The parameters used in our model calibration are summarised in Table 2. Note that c is the only free parameter that is undetermined by experimental measurement or literature values. However, we fix $c = 1$ W m^{-2} K^{-1} as our results are insensitive to typical variations in c. We explain the physical mechanisms related to this insensitivity further in Section 4.2.

Analysis of the experimental thermocouple data demonstrates that a significant amount of heat is lost during transfer of the ash from the oven to the experimental apparatus. This heat loss, which increases for thinner ash layers (see Figure 6), imparts an initial thermal profile in the ash that must be accounted for in an accurate calibration. We implement this in our model using a quadratic thermal initial condition in the ash based on the maximum temperature measured by each internal thermocouple. Specifically, we use an unconstrained multidimensional nonlinear minimization algorithm (Nelder & Mead, 1965) to find the quadratic coefficients that correspond to a minimised total residual between the initial condition and the maximum thermocouple temperatures. This quadratic profile accounts for both pre-experiment heat loss and the initial thermal gradients that redistribute heat throughout the system.

We compare our calibrated model with experimental data in Figure 4, which shows the thermal evolution within the ash, and in Table 3, which lists the proportion of melting after 10 minutes. Note that we present percentage melting values to avoid introducing arbitrary length scales into our 1-D model results. We find that for all ash thicknesses, our model can accurately simulate the measured thermal behaviour of the system. Our simulations accurately recover the magnitude and timescale of heat loss within the ash. Moreover, our calibrated model predicts melting values consistent with those observed in the laboratory. Our calibration performs best for progressively thinner ash layers. The growth of these small errors with ash thickness can be attributed to several effects: (1) maximum experimental temperatures are measured at progressively later times for thicker ash layers. Therefore, our assumed initial condition is more appropriate as d decreases. (2) The basal insulating boundary condition (Equation (4)) is typically valid provided that $(\rho_I c_I H_0)/(\rho_a c_A d) \gg 1$. For thicker ash layers the total thermal capacity of each phase becomes comparable, meaning that boundary effects begin to impact the dynamics of the system. (3) The reduced thermal capacity of thinner ash layers

	Symbol	Value
Ice parameters		
Density	ρ_I	916 kg m^{-3}
Specific heat capacity	$C_{p,I}$	2050 J kg^{-1} K^{-1}
Thermal conductivity	k_I	2.22 W m^{-1} K^{-1}
Latent heat of melting	L	333.55 J kg^{-1}
Melting temperature	T_m	273 K
Initial temperature	$T_{0,I}$	253 K
Ash parameters		
Density	ρ_A	2200 kg m^{-3}
Specific heat capacity	$C_{p,A}$	1201 J kg^{-1} K^{-1}
Thermal conductivity	k_A	1.37 W m^{-1} K^{-1}
Atmospheric heat loss coefficient	c	1.0 W m^{-2} K^{-1}

Table 2. Calibrated model parameters. Note that $C_{p,A}$ and k_A are mean values from five laboratory measurements.

d [mm]	H_0 [mm]	**Melt [%] Experiment**	**Melt [%] Modelled**
(a) 20	24.4	34.5	35.5
(b) 34	26.1	43.7	45.4
(c) 45	28.2	48.8	42.6

Table 3. Measured and simulated melt after 10 minutes. Note the labels (a), (b) and (c) correspond to the subplots in Figure 4.

induces less melting. Therefore, we expect that our model, which does not incorporate dynamic effects related to meltwater, to be more valid for thinner layers. (4) Due to the increased total thermal capacity of ash, steam generation increases with d. For ash temperatures below 400°C, steam generation is negligible in Ruapehu ash samples. However at higher temperatures, and when $(\rho_I c_I H_0)/(\rho_a c_A d) = O(1)$ or smaller, the latent heat of vaporization becomes non-negligible to the total thermal balance of the system.

Note that the melting results presented at the experimental scale represent a 'snapshot' of the melting dynamics. The end state or total melting (i.e. when ds/dt = 0) is defined as $s_\infty = \lim_{t\to\infty} s(t)$. For melting to terminate, the ash must lose sufficient heat to balance the flux terms in the Stefan condition. This is expected at the geophysical scale where typically $d \ll H_0$. In this regime, where melting is expected to be negligible relative to the initial thickness of ice (i.e. $-s_\infty/H \ll 1$), our model calibration performs best. Naturally, this motivates the use of our calibrated model at geophysical length scales to investigate the evolution of potentially hazardous melt generation following the emplacement of hot ash onto ice.

4.2 Geophysical scale melting

Based on published observations of volcanic deposits, 10s of centimetres of hot ash are expected to be deposited on metres of ice, e.g. Pierson et al. (1990) and Kilgour et al. (2010). Using the calibrated parameters in Table 2 we explore a reference scenario at a scale of $d = 0.1$ m and $H_0 = 1$

Dimensionless parameter	Symbol	Value
Diffusivity ratio	R_α	2.28
Conductivity ratio	R_k	1.62
Nusselt number	Nu	0.073
Lengthscale ratio	H	10

Table 4. Dimensionless reference parameters used for analysis of geophysical scale melting.

m and an initial uniform ash temperature of 200°C. The corresponding dimensionless parameters are listed in Table 4.

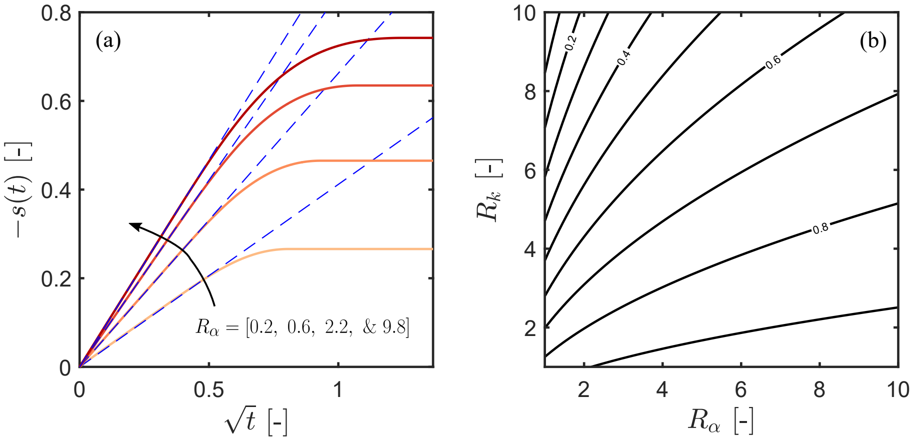

Figure 6. (a) Evolution of the ash-ice interface plotted for various values of R_α. The interface initially obeys the early-time similarity solution (dashed blue curves) $s = -\lambda\sqrt{t}$ before transitioning to an end state where melting terminates. (b) Contours of λ (equation (11)) are plotted to demonstrate its dependence on R_α and R_k.

At geophysical length scales, melting occurs in two distinct regimes (Figure 6): early-time diffusive motion of the ash-interface, before a transition to a late-time regime when melting terminates. Both of these regimes are relevant to volcanic hazards: the former governs the rate of meltwater supply; while the latter describes the magnitude of melt generation. Before considering the late time regime, we describe the early-time transient behaviour. In this regime, melting obeys the classical Stefan problem (e.g., Meirmanov, 2011) and permits the derivation of a similarity solution for the motion of the ash-ice interface:

$$s(t) = -\lambda\sqrt{t}, \tag{9}$$

where λ is a constant that determines the early-time melting rate. At early-times, the motion of the ash-ice interface is invariant to the length scales d and H_0, which allows for the derivation of analytic expressions for temperature in the ash and ice region respectively:

$$T = T_m + \frac{(T_A - T_m)\left(\mathrm{erf}(-\lambda/2) + \mathrm{erf}(\xi/2)\right)}{\mathrm{erf}(-\lambda/2) + 1}, \qquad \text{for } z > s(t), \tag{10a}$$

$$T = T_m + \frac{(T_I - T_m)\left(\mathrm{erf}(-\lambda/(2\sqrt{R_\alpha})) + \mathrm{erf}(\xi/(2\sqrt{R_\alpha}))\right)}{\mathrm{erf}(-\lambda/(2\sqrt{R_\alpha})) - 1}, \qquad \text{for } z < s(t), \tag{10b}$$

where T_A and T_I are the initial ash and ice temperatures respectively, $\xi = z/\sqrt{t}$ is a diffusive coordinate transform, and $\mathrm{erf}(\cdot)$ is the error function. Differentiating these analytical expressions before substituting into the Stefan condition (Equation 8c) yields an expression for λ, which is given by the solution to

$$\frac{\lambda}{2} = \frac{R_k(T_m - T_I)e^{-\frac{\lambda^2}{4R_\alpha}}}{\sqrt{\pi R_\alpha}\left(\mathrm{erf}\left(\frac{\lambda}{2\sqrt{R_\alpha}}\right)+1\right)} + \frac{(T_A - T_m)e^{-\frac{\lambda^2}{4}}}{\sqrt{\pi}\left(\mathrm{erf}\left(\frac{\lambda}{2}\right)-1\right)}. \tag{11}$$

We solve Equation (11) using `MATLAB's` nonlinear root finding algorithm `fzero`. We demonstrate the accuracy of our numerical scheme by overlaying these similarity solutions for different values of R_α in Figure 6(a). The similarity solution's independence of length scales means that the early-time melting rate is determined by the interplay between R_α, R_k, T_m, T_I and T_A only. Solving Equation (11) allows for efficient exploration of this parameter space. Given that the principal temperatures trivially modulate the initial melting rate (e.g. λ monotonically increases with T_A), we consider the impact of R_k and R_α in Figure 6(b). Here we show that λ monotonically increases and decreases with R_α and R_k respectively. Increasing R_k linearly increases the first term in Equation (8c), which reduces the strength of melting by decreasing the heat flux differential across the ash-ice interface. The melting rate increases with R_α due to the increased relative strength of thermal diffusion in the ice. Furthermore, by reducing the relative strength of thermal diffusion in the ash, convective heat losses to the atmosphere are transmitted to the ash-interface at a slower rate, thus delaying the transition from early-time self similar melt propagation to late-time termination of melting (see below).

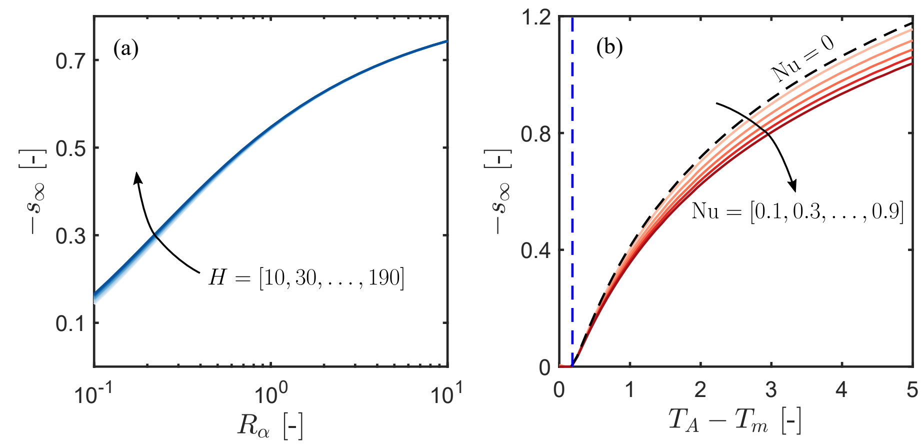

Figure 7. End state position of the ash-ice interface vs (a) R_α, with several different thickness ratios plotted to demonstrate the invariance of total melting to H; (b) Difference in ash and melting temperature $T_A - T_m$, also plotted for various values of Nu which highlights the weak dependence on the Nusselt number. The dashed black and blue curves represent the Nu = 0 limit and melting threshold (see equation (12)) respectively.

At intermediate-times, the motion of the ash-ice interface deviates from the early-time $s \propto \sqrt{t}$ scaling towards a late-time state (s_∞) when melting stops. This transition develops as convective heat losses at $\eta = 1$ begin to impact thermal diffusion across the ash-ice interface. Eventually, the ash has lost sufficient heat that the heat fluxes across the ash-ice interface balance and melting terminates. Accordingly the ash-ice interface will remain motionless unless provided with latent heat to resume melting. At intermediate- and late-times, thermal transport and associated motion of the ash-ice interface, is coupled to the inherent length scales of the system, and also to the parameters that govern the rate of heat loss within the system. The impacts of select parameters (R_α, H, $T_A - T_m$, and Nu) on the total (i.e. end state) melt production are illustrated in Figure 7. As in the early-time regime, increasing R_α, which strengthens thermal diffusion in the ice, results in increased total melting (Figure 7(a)). For relevant geophysical settings where $H \gg 1$, $|s_\infty|$ is invariant to the ice thickness (Figure 7a). This is because, when melting is small relative to the initial ice thickness, heating of the ice remains confined away from the basal boundary which therefore does not impose any scale effects on the total melt production. In Figure 7(b) we highlight the impact of the ash temperature and Nusselt number on s_∞. Intuitively, $|s_\infty|$ monotonically increases with the ash temperature above a threshold temperature which is required to supply latent heat across the ash-ice interface. This threshold is derived by setting $\lambda = 0$ in Equation (11), which yields

$$T_A - T_m > \frac{R_k(T_m - T_I)}{\sqrt{R_\alpha}}. \tag{12}$$

We also demonstrate that, relative to other dimensionless parameters, the Nusselt number has a limited impact on the total melt production. By strengthening convective heat losses to the atmosphere (increasing Nu), melt generation reduces, but only by a small fraction. This relative insensitivity to Nu is because thermal transport in the ash is dominated by conduction into the ice. This is expected for $0 < Nu < 1$, and further explains the insensitivity to Nu in our model calibration. Note also that as the experiments have not reached end state melting, and therefore as Equation (11) is invariant to Nu we expect our calibration to be insensitive to variations in the Nusselt number. In Figure 7(b) our reference case (Nu $\sim$ 0.073) will lie between the dashed black and uppermost orange curves. The proximity of our reference case to the convection free (Nu = 0) limit demonstrates that convective heat losses to the atmosphere are essentially negligible over the time scale of melting for typical geophysical parameters and temperatures considered.

5 Discussion

When PDCs are emplaced onto snow and ice substrates, they rapidly transfer heat from the particle layer into the substrate due to large temperature gradients between the two mediums. This heat transfer generates melt and steam which can be incorporated into the flow transforming it, in terms of both its mobility and character. The role of melt and steam in PDC-ice interactions differ, as do their production timescales. Melting is a continuous process for as long as i) the hot ash can supply latent heat (via a difference in heat flux across the ash-ice interface), and ii) there is a supply of ice to melt. The production and incorporation of melt can cause a PDC to transform from a dry granular flow into a saturated, sediment-laden flow, termed an ice-melt lahar (Thouret et al., 2007). Steam production on the other hand, is dependent on the initial temperature gradient and the thermal mass of the particles in contact with the ice. Steam production stops when particles are no longer able to heat the water above its vaporisation temperature. The production of steam in PDC-ice interactions can result in fluidisation of the particle layer, causing convective overturning of the layer, and increasing its overall mobility.

In natural volcanic settings PDCs scour the ice thermally and mechanically, but before the physical coupling between the thermal and mechanical mechanisms can be considered, the thermal interactions must first be isolated. In the previous sections we present a series of systematic static melting experiments, along with a calibrated 1-D numerical model and mathematical analysis to resolve the rate of heat transfer from a static hot particle layer to an ice substrate, and to quantify melt. The model can be used to derive a time-series of melt generation (see Section 5.3). From this, we can generate ice-melt lahar source hydrographs, which can be used as an input in surface flow hazard models. From here on, we discuss heat transfer in particle-ice interactions, including the generation and role of melt and steam. We also consider insights from our experiments and how the 1-D model can be applied at geophysical scales, including constraining the ice-melt lahar hazard. Finally, we review the limitations of this investigation and suggest recommendations for further work.

5.1 Heat transfer in particle-ice interactions

We conducted a series of static melting experiments, where a layer of hot particles were emplaced onto a horizontal ice layer to investigate heat transfer from particle to ice, as an analogue to the thermal interactions between hot pyroclasts and ice. Our 1-D model simulates heat transfer between two solid phases, i) a hot ash layer, and ii) an underlying ice layer. The model is calibrated to $200°C$ Ruapehu experiments. Our experiment data provided two constraints for the model, i) the time evolution of temperature through the particle layer, and ii) a mass of melt at the end of the 10 minute experiment. In all experiments the thermocouples recorded an initial spike in the temperature as particles were emplaced onto the ice, followed by subsequent gradual cooling as heat was transferred from the particle layer into the ice substrate. Our model captures the magnitude and timescale of the heat loss from the ash. With our geophysical extension this model can be used to determine the cooling timescales of deposited pyroclastic material.

5.2 Melt and steam generation in particle-ice interactions

The heat transfer from the particle layer to the ice substrate initiates the production of melt and steam. The quantities of melt and steam produced in experiments were determined by the particle type, initial particle temperature, and layer thickness. Ballotini and Ruapehu ash experiments produced comparable quantities of melt, but ballotini particles produced more steam. Pumice experiments produced the least melt and negligible steam at all temperatures investigated. We note that steam generation was not present in all experiments, and was negligible for all cases where the particles were initially cooler than 400 °C. For natural samples with $T_A(t = 0, z) > 400$ °C the bulk of ice that is melted or evaporated is measured to be in the liquid phase (Figure 5d); meaning that, melting is the dominant phase transition over the range of temperatures experienced during PDC emplacement. Therefore for simplicity, higher-order terms related to vaporisation are not included in our 1-D model. Our numerical model successfully predicts melt generation to c.5% where steam production is negligible (Table 3). With our geophysical extension, we can predict melt generation at geophysical scales and provide a time-series of this melt generation. This informs ice-melt lahar genesis, which is discussed further in Section 5.3.

5.2.1 Melt

In experiments melt systematically increased with initial particle temperature and layer thickness. The melt data showed a reduction in the rate of increase in melt with increasing particle layer thickness for all particle types (Figure 5). We propose two potential explanations for this melt curve flattening. Firstly, the observed flattening could result from the limited timescale of the experiment such that heat from particles in the upper region of a thick particle layer did not have time to transfer heat to the particle-ice interface. Secondly, the observed flattening relates to changes in the partitioning of energy within the system with increasing particle layer thickness. With thinner particle layers the heat energy melted the underlying ice layer and caused a single phase change from ice to meltwater. With thicker particle layers the increased heat energy can be expended through i) heating of meltwater to higher temperatures, and ii) meltwater vapourisation. The ratio of this energy partitioning will depend on the initial experiment conditions, including particle layer thickness and temperature. The particle type (and so particle porosity and thermal conductivity) matters too; for example, all experiments with pumice particles produced negligible steam.

Temperature data from the experiments also provided insights into the movement of melt through the particle layer. In several experiments, a stepped reduction in particle temperature followed by temperature stabilisation was recorded by the thermocouples. We interpreted this to be an upward-moving meltwater front. This meltwater front was cooler than the dry particles, which caused a step in the temperature profile as the thermocouple came into contact with the melt, and a stabilisation as the pore space surrounding the thermocouple became occupied by melt. These stepped reductions in temperature were recorded by sequentially higher thermocouples as the meltwater front rose through the particle layer. We observed these meltwater fronts for all three particle types, and rates of movement ranged from 0.04-0.59 mm/s. An example of these stepped temperature profiles can be seen in Figure 4c. As our model does not include a fluid phase, it cannot capture these perturbations. However, our model performs well at reproducing the leading-order thermal decay measured in the experiments.

We propose that the principal mechanism of this upward-moving wetting front is particle sinking, displacing ponded ice-surface melt which is generated from the downward wasting of the ice layer. Walder (2000b) similarly reported on the presence of an upward-moving meltwater front as particles passively melted into the underlying snow. We tested this hypothesis for ballotini based on the well-established random close packing of spheres, where 63.66% volume is spheres and 36.34%

volume is pore space (G. D. Scott & Kilgour, 1969). The ballotini experiment with a 45 mm particle layer thickness and an initial temperature of 200°C produced 72.1 g melt during the experiment, equivalent to 16.76 mm melt within our experiment apparatus if no particles were present. Taking into account the assumed random close packing of spheres and conservation of mass, this calculation produces a meltwater height of 46 mm, which exceeds the particle layer thickness by 1 mm. We observed melt ponding above the particle surface in this experiment. An additional mechanism for the upward transport of meltwater, relating to steam escape, is discussed in section 5.2.2.

5.2.2 Steam

For simplicity, we do not include higher-order terms related to steam generation in our numerical model. It remains important however to understand the role of steam in PDC-ice interactions, in terms of both flow mobility and character, as PDC emplacement temperatures can be higher than the temperatures required to generate steam, e.g. Mount St. Helens (Banks & Hoblitt, 1996), and Soufrière Hills Volcano (Cole et al., 2002; A. C. Scott & Glasspool, 2005). Initial particle temperatures in some experiments were sufficiently high to generate steam, revealing a range of additional behaviours pertaining PDC-ice interactions. High temperature experiments revealed the existence of i) steam-driven melt incorporation, and ii) fluidisation and elutriation of fines. Evidence for the presence of steam in experiments was recorded by the thermocouple data in the form of i) data noise, and ii) stability in the temperature profile around 100°C. Additional evidence was provided through experiment footage (see Supplementary Material).

Several features observed during the experiments and in the resulting data provided evidence of steam-driven melt incorporation into the particle layer. Within the first few seconds of some high temperature experiments, we observed vapour-supported melt lenses skittering on the particle surface. After a few seconds the vapour bubbles burst, leaving a saturated area on the particle surface. Thermocouple data indicates that this boiling is occurring at or close to the particle-ice interface as the data show sustained temperature stability around 100°C in the thermocouples closest to the ice. This steam-driven melt mixing observation is also consistent with observations by Walder (2000b), who reported that under some conditions steam generation can cause complete convective overturning of the particles, which drives thermal scouring of the substrate, mixing, and slurry formation.

The thermocouple data provide further evidence for steam-driven melt mixing. Where steam escaped through the particle layer the temperature profile steps were recorded at multiple successive thermocouples simultaneously. The negligible time between these drops in temperature at successive thermocouple heights suggests that steam escape drives efficient transport and mixing of melt through the particle layer. This steam escape was also recorded within experiment footage as localised ‘flash’ wetting of the particle surface. The thermocouple data, in combination with observations highlight the important role of steam for efficient melt incorporation and mixing within the particle layer.

Fluidisation of the particle layer under varied initial temperature and layer thickness conditions for all three particle types was observed. Fluidisation occurs when the upward flux of gas is sufficient to support the weight of the particles above, reducing interparticle contacts, causing the layer to behave in a fluid-like manner (R. S. J. Sparks, 1976). Fluidisation of the particle layer will have an influence on flow mobility in dynamic particle-ice interaction settings. In experiments fluidisation occurred instantaneously following emplacement, and endured for several seconds. Ballotini particles were most readily fluidised across the widest range of initial conditions. This is consistent with the inferred measurements of steam being greatest for ballotini particles.

Where fluidisation occurred in Ruapehu ash experiments, fines were elutriated from the particle layer and spattered up the beaker sides. Evidence for fines elutriation is recorded in PDC deposits in the form of fines depletion (Brand et al., 2014) and elutriation pipes (Pacheco-Hoyos et al., 2020; Stinton et al., 2014). The presence of this phenomenon in the experiments, highlights that the initial particle temperature range in experiments was sufficient to reproduce naturally occurring behaviours.

Although steam generation is not present in all experiments, nor accounted for in our model, the importance of steam in terms of particle layer mobility and melt incorporation through the particle layer has been elucidated. Extrapolating these observations to dynamic settings and geophysical scales, we anticipate that the presence of steam may increase the mobility and potential runout distances of PDCs, and accelerate the transformation from PDC to ice-melt lahar.

5.3 Geophysical scale melting and constraining the ice-melt lahar hazard

When hot pyroclastic material is emplaced onto ice substrates during volcanic eruptions, it can thermally and mechanically scour the substrate, generating and incorporating steam and melt into the granular layer. Where melt supply is limited and incorporation predominantly consists of eroded frozen matter, the PDC can transform into a mixed avalanche (Pierson & Janda, 1994; Lube et al., 2009; Breard et al., 2020). If sufficient melt is generated and mixing occurs, this layer can transform from hot, dry granular matter, to a saturated, sediment-laden flow, or ice-melt lahar (Major & Newhall, 1989; Pierson et al., 1990; Kilgour et al., 2010; Waythomas, 2014).

Ice-melt lahars have historically represented some of the most hazardous volcanic flows (Brown et al., 2017). During the 1985 eruption of Nevado del Ruiz, Colombia, PDCs were emplaced onto the summit area resulting in thermal and mechanical scour of the snow and ice substrate, removing 16% of the surface area and 9% of the total volume of the summit ice cap (Thouret, 1990). The incorporation of melt, snow, and ice into these PDCs transformed them into ice-melt lahars that flowed down valleys on the volcano flanks. The propagation of these lahars through populated areas resulted in c.25,000 fatalities (Naranjo et al., 1986), highlighting the extreme hazards posed by PDC-ice interactions and ice-melt lahars, and the need for robust modelling of these events.

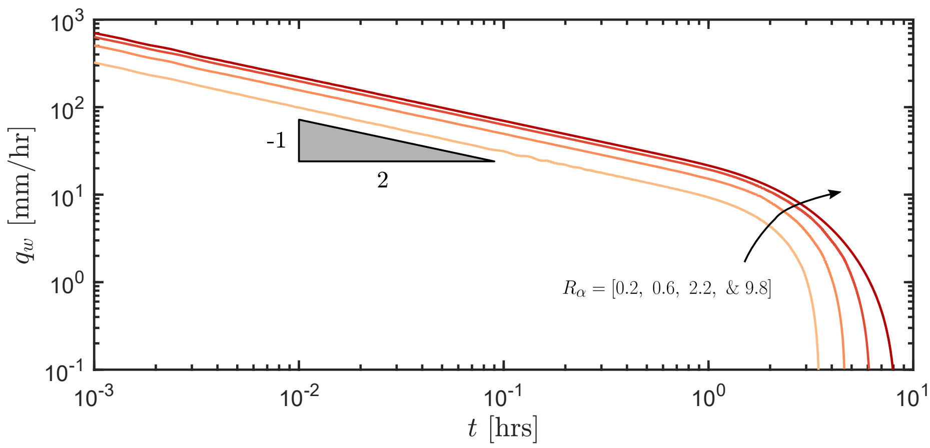

Figure 8. Example hydrographs calculated by dimensionalising the curves in Figure. 6(a). Note that early-time melting produces a meltwater flux that decays with $q_w \sim 1/\sqrt{t}$.

Our experiments and numerical model provide constraints on the magnitude and timescales of melting in PDC-ice interactions. This can be used to inform source conditions for the generation of ice-melt lahars. Physics-based simulations of lahars (and other debris flows) used in hazard assessment typically use volumetric flux $[L^3/T]$ hydrographs as source conditions, which provide time-series fluxes of water and entrained solids (e.g., Jenkins et al., 2023). This source flux is typically distributed over an area A $[L^2]$, meaning that the prescribed flux has units $[L/T]$. In cases of deposition of hot, static ash, our model can provide a time-series of melt generation. Given that $-s(t)$ represents the total melt $[L]$ generated in a time t, the meltwater flux q_w $[L/T]$ is given by

$$q_w = \frac{\rho_w}{\rho_I}\frac{\mathrm{ds(t)}}{\mathrm{dt}}, \tag{13}$$

where ρ_w is the water density. In Section 4.2, we established that the early-time motion of the ash-ice interface obeys $s \sim \lambda\sqrt{t}$. Substituting this into Equation (13) and taking $\rho_w/\rho_I \approx 1$ yields the early-time form of the meltwater flux, which obeys $q_w(t) \sim \lambda/(2\sqrt{t})$. In Figure 8 we plot redimensionalised hydrographs that correspond to the simulations show in Figure 6. Here, the meltwater flux decay follows the $q_w \propto 1/\sqrt{t}$ early-time scaling, before sharply tending towards $q_w \to 0$ at later times as melting terminates. Melting occurs over nearly 10 hours, and the magnitude and duration of q_w exceeds well-established empirical thresholds for analogous rainfall-driven debris flows (e.g., Guzzetti et al., 2008). By combining hydrographs generated by our model with calibrated empirical thresholds for lahar/debris flow initiation, insights can be provided into the triggering conditions of melt-driven lahars. Furthermore, where melt-driven lahar genesis is expected, our model provides a physical basis for the general form of melt-driven source hydrographs. Note that a slight perturbation is required to avoid a singularity in q_w at $t = 0$. However, morphodynamic flow solvers typically require a short 'ramp-up' period to avoid instabilities in the source region.

5.4 Limitations and recommendations for further work

In the static melting experiments, we investigated the interactions between hot granular media and ice. In nature, where PDCs are emplaced onto frozen substrates, the substrate surface will typically be comprised of varying thicknesses of less-dense snow, and underlain by ice. We used ice in our experiments for two reasons: i) snow is difficult to reproduce in a laboratory environment, and ii) ice is a less complex substance and efforts were made to simplify the research problem for modelling purposes. Further research into PDC interactions with frozen substrates should consider how heat transfer, melt and steam generation would differ if the substrate consisted of snow, rather than ice. The experimental works of Walder (2000a,b) investigated hot particle-snow interactions and provided useful insights into thermal scour of snow substrate by convective vapour bubbling, and passive melting at lower temperatures. However, this research did not quantify the rate of heat transfer, or the generated melt and steam, limiting comparison with our numerical model.

Similar to Walder (2000b), our experiments isolated the thermal interactions between particle and ice, and did not account for mechanical shear, which exists in natural PDC-ice interaction settings. By isolating thermal interactions, the rate of heat transfer from particle to ice was quantified, as well as melt and steam generated when a hot particle layer is instantaneously emplaced onto ice. Isolating the thermal interactions, in absence of mechanical shear motion was important as in natural PDC-ice interaction settings, i) not all emplaced particles will be set in motion, and therefore some passive melting will occur, and ii) the dynamics and timescales of melt and steam generation were unknown without the static melting experiments. We have conducted further experiments to investigate hot particle-ice interactions in dynamic flow configurations, including i) granular collapse over horizontal frozen substrates, and ii) granular flow over ice in an inclined plane configuration, revealing complex interactions between the particle layer and substrate, as well as interparticle interactions, particularly with varying quantities of melt and steam incorporation. The static experiments were an important precursor to these investigations from phenomenological and numerical perspectives, but the extension to dynamic configurations provides insights into the thermal and mechanical coupling when hot granular media is emplaced onto and flows over ice.

For simplicity we did not include higher-order terms related to steam generation in our numerical model. Nevertheless, the model was able to accurately reproduce the leading order dynamics measured in the experiments. However, we do not consider this to be an insurmountable limitation as there are no means to quantify steam in natural PDC-ice interactions, and steam generation at geophysical scales using the ratio of melt to steam generation in the small-scale laboratory experiments under different initial conditions can be estimated. At geophysical scales, it is most critical that i) ice melt volume generated under different initial conditions based on PDC volume can be quantified, and the implications for this in terms of ice-melt lahar generation are understood, and ii) the physical role of steam in terms of melt incorporation, and its effects on flow mobility and character are understood. The experiments in combination with the numerical model work to resolve these requirements.

6 Conclusions

We conducted a series of static melting experiments, where hot particles were emplaced onto an ice substrate as an analogue to PDC-ice interactions. These experiments isolated the thermal interactions, as in order to fully understand the thermal and mechanical coupling in PDC-ice interactions, we must first generate a detailed physical knowledge of particle-ice interactions in the simplest configuration. Our experiments revealed that melt and steam systematically increase with increasing particle temperature and layer thickness. The experiments were capable of reproducing natural volcanic phenomena, including fluidisation and fines elutriation, indicating that the initial temperature conditions were within a representative natural range. Experiments also provided insights into melt mixing mechanisms. Based on the thermocouple data, in combination with visual observations we determined that steam plays a critical role in the rate of melt incorporation through the particle layer. This has implications for the rate of transformation from PDC to ice-melt lahar.

We also presented a 1-D numerical model of heat transfer, calibrated against Ruapehu ash experiments. This model accurately predicts melt generation to within c.5%. We also provided analytical similarity solutions for our numerical model at early-times and at typical geophysical scales, along with an example meltwater flux hydrograph which can be used to inform source conditions for simulations of melt-driven lahars. The ability to predict melt generation at geophysical scales when a PDC is emplaced onto an ice substrate represents a significant advancement towards robust modelling of the ice-melt lahar hazard.

We have conducted further experimental work to investigate hot granular flows on ice at an incline. The experimental and numerical simulations presented in this paper in conjunction with the dynamic inclined plane experiments will form key input parameters in the topographically-forced surface flow hazard model, LaharFlow, enabling modelling of PDCs over ice substrates, and their transformation into ice-melt lahars. This model will have wide-reaching applications in regions affected by glaciovolcanic hazards.

7 Open Research

The experiment temperature, melt and steam data, along with executable matlab codes and numerical simulation data reported within this study are freely available in a Zenodo repository via DOI: 10.5281/zenodo.8278922 (Vale et al., 2023).

Acknowledgments

ABV acknowledges the support from a University of Bristol Postgraduate Scholarship and industrial sponsor GNS Science. LTJ acknowledges funding from the UKRI Global Challenges Research Fund grant NE/S009000/1. JCP acknowledges the support of a University of Bristol Research Fellowship. LTJ, JCP, and AJH acknowledge a University of Bristol Research project 'From Everyday to Extreme: Strengthening Resilience to Frequent Flash Floods in Perú'. GK and AS are supported by the New Zealand Ministry of Business, Innovation and Employment (MBIE) through the Hazards and Risk Management programme (Strategic Science Investment Fund, contract C05X1702). The authors also gratefully acknowledge insightful conversations with J. Walder and J. Cowlyn.

Appendix A Bilinear remapping of the numerical model

A common approach in obtaining numerical solutions to moving boundary problems is to rescale the governing equations onto a fixed domain. Although introducing additional mathematical complexity (in the form of advective transport terms), solving advection-diffusion problems on a fixed domain removes numerical complexities associated with solving coupled PDEs on evolving domains (e.g., time-dependent grids and resolution). Bilinear mapping is adopted. That is, a separate linear transform is applied to each solid phase. The location of key interfaces in these rescaled domains (η

for ash, ν for ice) are summarised in the table below. These rescaled domains are solved separately and coupled together through a shared Direchlet boundary condition for temperature and the Stefan condition, which scale advective terms that account for the motion of the ash-ice interface.

	z	η
Air-Ash	$1 + s(t)$	1
Ash-Ice	$s(t)$	0
	z	ν
Ash-Ice	$s(t)$	0
Ice-Rock	$-H_0$	-1

A1 Remapping the ash subdomain $z \iff \eta$

The ash subdomain is rescaled using the linear mapping

$$\eta = z - s. \tag{A1}$$

Accordingly, the spatial and temporal derivatives from independent variables (z, t) to (η, t) must be transformed. The transformed first and second spatial derivatives are

$$\left.\frac{\partial}{\partial z}\right|_t = \left.\frac{\partial \eta}{\partial z}\right|_t \frac{\partial}{\partial \eta} = \frac{\partial}{\partial \eta}, \tag{A2}$$

and

$$\left.\frac{\partial^2}{\partial z^2}\right|_t = \left.\frac{\partial \eta}{\partial z}\right|_t \frac{\partial}{\partial \eta}\frac{\partial}{\partial \eta} = \frac{\partial^2}{\partial \eta^2}. \tag{A3}$$

Finally, the transformed temporal derivative is given by

$$\left.\frac{\partial}{\partial t}\right|_z \Rightarrow \left.\frac{\partial}{\partial t}\right|_\eta + \left.\frac{\partial \eta}{\partial t}\right|_z \left.\frac{\partial}{\partial \eta}\right|_t = \frac{\partial}{\partial t} - \frac{\partial s}{\partial t}\frac{\partial}{\partial \eta}. \tag{A4}$$

A2 Remapping the ice subdomain $z \iff \nu$

The same procedure is now performed in the ice region, which is rescaled using the linear mapping:

$$\nu = \frac{z - s}{H + s}, \tag{A5}$$

whose first and second spatial derivatives are

$$\left.\frac{\partial}{\partial z}\right|_t = \left.\frac{\partial \nu}{\partial z}\right|_t \frac{\partial}{\partial \nu} = \frac{1}{H + s}\frac{\partial}{\partial \nu}, \tag{A6}$$

and

$$\left.\frac{\partial^2}{\partial z^2}\right|_t = \left.\frac{\partial}{\partial z}\right|_t \left[\frac{1}{H + s}\frac{\partial}{\partial \nu}\right] = \frac{1}{(H + s)^2}\frac{\partial^2}{\partial \nu^2}. \tag{A7}$$

The transformed temporal derivative is given by

$$\left.\frac{\partial}{\partial t}\right|_z \Rightarrow \left.\frac{\partial}{\partial t}\right|_\nu + \left.\frac{\partial \nu}{\partial t}\right|_z \left.\frac{\partial}{\partial \nu}\right|_t = \frac{\partial}{\partial t} - \left(\frac{1 + \nu}{H + s}\right)\frac{\partial s}{\partial t}\frac{\partial}{\partial \nu}. \tag{A8}$$

Applying these transformed spatial and temporal derivatives to each subdomain yields our system of rescaled, non-dimensional governing Equations (8a-d).

References

Ahmed, S., John, S. E., Šutalo, I. D., Metcalfe, G., & Liffman, K. (2012). Experimental study of density segregation at end walls in a horizontal rotating cylinder saturated with fluid: Friction to lubrication transition. *Granular Matter*, *14*. doi: 10.1007/s10035-012-0335-2

Antriasian, A., & Beardsmore, G. (2014). Longitudinal heat flow calorimetry: A method for measuring the heat capacity of rock specimens using a divided bar. *Geotechnical Testing Journal*, *37*. doi: 10.1520/GTJ20130168

Antriasian, A. M. (2009). The Portable Electronic Divided Bar (PEDB): a Tool for Measuring Thermal Conductivity of Rock Samples Thermal Conductivity and Heat Flow Calculation of Thermal Conductivity. In *Australian geothermal energy* (pp. 1–6).

Banks, N. G., & Hoblitt, R. P. (1996). *Direct temperature measurements of deposits, Mount St. Helens, Washington, 1980-1981* (Tech. Rep.). U.S. Geological Survey. doi: 10.3/JQUERY-UI.JS

Belousov, A., Voight, B., Belousova, M., & Petukhin, A. (2002). Pyroclastic surges and flows from the 8-10 May 1997 explosive eruption of Bezymianny Volcano, Kamchatka, Russia. *Bulletin of Volcanology*, *64*, 455–471.

Brand, B. D., Mackaman-Lofland, C., Pollock, N. M., Bendaña, S., Dawson, B., & Wichgers, P. (2014). Dynamics of pyroclastic density currents: Conditions that promote substrate erosion and self-channelization - Mount St Helens, Washington (USA). *Journal of Volcanology and Geothermal Research*, *276*, 189–214. doi: 10.1016/J.JVOLGEORES.2014.01.007

Branney, M. J., & Gilbert, J. S. (1995, 11). Ice-melt collapse pits and associated features in the 1991 lahar deposits of volcán hudson, chile: criteria to distinguish eruption-induced glacier melt. *Bulletin of Volcanology 1995 57:5*, *57*, 293-302. Retrieved from `https://link.springer.com/article/10.1007/BF00301289` doi: 10.1007/BF00301289

Breard, E. C. P., Calder, E. S., & Ruth, D. C. S. (2020). The interaction between concentrated pyroclastic density currents and snow: a case study from the 2008 mixed-avalanche from Volcán Llaima (Chile). *Bulletin of Volcanology*, *82*(75). doi: 10.1007/s00445-020-01413-4

Brown, S. K., Jenkins, S. F., Stephen, R., Sparks, J., Odbert, H., & Auker, M. R. (2017). Volcanic fatalities database: analysis of volcanic threat with distance and victim classification. *Journal of Applied Volcanology*, *6*(15). doi: 10.1186/s13617-017-0067-4

Buckland, H. M., Saxby, J., Roche, M., Meredith, P., Rust, A. C., Cashman, K. V., & Engwell, S. L. (2021). Measuring the size of non-spherical particles and the implications for grain size analysis in volcanology. *Journal of Volcanology and Geothermal Research*, *415*(107257). doi: 10.1016/j.jvolgeores.2021.107257

Cole, P. D., Calder, E. S., Druitt, T. H., Hoblitt, R., Robertson, R., Sparks, R. S., & Young, S. R. (1998). Pyroclastic flows generated by gravitational instability of the 1996-97 lava dome of Soufriere Hills Volcano, Montserrat. *Geophysical Research Letters*, *25*(18), 3425–3428. doi: 10.1029/98GL01510

Cole, P. D., Calder, E. S., Sparks, R. S., Clarke, A. B., Druitt, T. H., Young, S. R., ... Norton, G. E. (2002). Deposits from dome-collapse and fountain-collapse pyroclastic flows at Soufrière Hills Volcano, Montserrat. *Geological Society Memoir*, *21*(1), 231–262. doi: 10.1144/GSL.MEM.2002.021.01.11

Cowlyn, J. D. (2016). *Pyroclastic density currents at Ruapehu volcano; New Zealand* (Unpublished doctoral dissertation). University of Canterbury.

Dellino, P., Dioguardi, F., Isaia, R., Sulpizio, R., & Mele, D. (2021). The impact of pyroclastic density currents duration on humans: the case of the AD 79 eruption of Vesuvius. *Scientific Reports*, *11*(1). doi: 10.1038/s41598-021-84456-7

Druitt, T. H. (1998). Pyroclastic density currents. *Geological Society Special Publication*, *145*, 145–182. doi: 10.1144/GSL.SP.1996.145.01.08

Druitt, T. H., Calder, E. S., Cole, P. D., Hoblitt, R. P., & Loughlins, S. (2002). Small-volume, highly mobile pyroclastic flows formed by rapid sedimentation from pyroclastic surges at Soufrière Hills Volcano, Montserrat: an important volcanic hazard. In *Geological society memoir* (pp. 263–279).

Fisher, R. V. (1995). Decoupling of pyroclastic currents: hazards assessments. *Journal of Volcanology and Geothermal Research*, *66*(1-4), 257–263. doi: 10.1016/0377-0273(94)00075-R

Flint, A. L., & Flint, L. E. (2002). 2.2 particle density. In J. H. Dane & C. G. Topp (Eds.), *Methods of soil analysis: Part 4 physical methods* (First ed., Vol. 5, p. 229-240). Soil Science Society of America.

Goudarzi, S., Mathias, S. A., & Gluyas, J. G. (2016). Simulation of three-component two-phase flow in porous media using method of lines. *Transport in Porous Media*, *112*(1), 1–19.

Guzzetti, F., Peruccacci, S., Rossi, M., & Stark, C. P. (2008). The rainfall intensity–duration control of shallow landslides and debris flows: an update. *Landslides*, *5*, 3–17.

Huggel, C., Ceballos, J. L., Pulgarín, B., Ramírez, J., & Thouret, J. C. (2007). Review and reassessment of hazards owing to volcano-glacier interactions in colombia. *Annals of Glaciology*, *45*. doi: 10.3189/172756407782282408

Jenkins, L. T., Creed, M. J., Tarbali, K., Muthusamy, M., Trogrlić, R. Š., Phillips, J. C., ... McCloskey, J. (2023). Physics-based simulations of multiple natural hazards for risk-sensitive planning and decision making in expanding urban regions. *International Journal of Disaster Risk Reduction*, *84*, 103338.

Kelfoun, K., & Gueugneau, V. (2022). A unifying model for pyroclastic surge genesis and pyroclastic flow fluidization. *Geophysical Research Letters*, *49*(5), e2021GL096517. doi: 10.1029/2021GL096517

Kilgour, G., Manville. V., Della Pasqua, F., Graettinger. A., Hodgson, K. A., & Jolly, G. E. (2010). The 25 September 2007 eruption of Mount Ruapehu, New Zealand: Directed ballistics, surtseyan jets, and ice-slurry lahars. *Journal of Volcanology and Geothermal Research*, *191*(1-2), 1–14. doi: 10.1016/J.JVOLGEORES.2009.10.015

Lerner, G. A., Cronin, S. J., & Turner, G. M. (2019). Evaluating emplacement temperature of a 1000-year sequence of mass flows using paleomagnetism of their deposits at Mt. Taranaki, New Zealand. *Volcanica*, *2*(1), 11–24. Retrieved from http://www.jvolcanica.org/ojs/index.php/volcanica/article/view/24 doi: 10.30909/VOL.02.01.1124

Liu, E. J., Cashman, K. V., Rust, A. C., & Höskuldsson, A. (2017). Contrasting mechanisms of magma fragmentation during coeval magmatic and hydromagmatic activity: the Hverfjall Fires fissure eruption, Iceland. *Bulletin of Volcanology*, *79*(68). doi: 10.1007/S00445-017-1150-8

Lube, G., Breard, E. C. P., Cronin, S. J., & Jones, J. (2015). Synthesizing large-scale pyroclastic flows: Experimental design, scaling, and first results from PELE. *Journal of Geophysical Research: Solid Earth*, *120*(3), 1487–1502. doi: 10.1002/2014JB011666

Lube, G., Cronin, S. J., & Procter, J. N. (2009). Explaining the extreme mobility of volcanic ice-slurry flows, Ruapehu volcano, New Zealand. *Geology*, *37*(1), 15–18. doi: 10.1130/G25352A.1

Major, J. J., & Newhall, C. G. (1989). Snow and ice perturbation during historical volcanic eruptions and the formation of lahars and floods: A global review. *Bulletin of Volcanology*, *52*, 1–27.

Meirmanov, A. M. (2011). *The stefan problem* (Vol. 3). Walter de Gruyter.

Microtrac MRB. (n.d.). *Particle Size & Particle Shape Analyzer: CAMSIZER X2.* Retrieved 2021-08-24, from https://www.microtrac.com/products/particle-size-shape-analysis/dynamic-image-analysis/camsizer-x2/function-features

Naranjo, J. L., Sigurdsson, H., Carey, S. N., & Ftrrz, W. (1986). Eruption of the nevado del ruiz volcano, colombia, on 13 november 1985: Tephra fall and lahars. *Science*, 961-963. Retrieved from http://science.sciencemag.org/

Nelder, J. A., & Mead, R. (1965). A simplex method for function minimization. *The computer journal*, *7*(4), 308–313.

Pacheco-Hoyos, J. G., Aguirre-Díaz, G. J., & Dávila-Harris, P. (2020). Elutriation pipes in ignimbrites: An analysis of concepts based on the Huichapan Ignimbrite, Mexico. *Journal of Volcanology and Geothermal Research*, *403*. doi: 10.1016/J.JVOLGEORES.2020.107026

Pierson, T. C., & Janda, R. J. (1994). Volcanic mixed avalanches: A distinct eruption-triggered mass-flow process at snow-clad volcanoes. *GSA Bulletin*, *106*(10), 1351–1358.

Pierson, T. C., Janda, R. J., Thouret, J. C., & Borrero, C. A. (1990). Perturbation and melting of snow and ice by the 13 November 1985 eruption of Nevado del Ruiz, Colombia, and consequent mobilization, flow and deposition of lahars. *Journal of Volcanology and Geothermal Research*, *41*(1-4), 17–66. doi: 10.1016/0377-0273(90)90082-Q

Roche, O., Gilbertson, M., Phillips, J. C., & Sparks, R. S. (2002). Experiments on deaerating granular flows and implications for pyroclastic flow mobility. *Geophysical Research Letters*, *29*, 40-1. doi: 10.1029/2002GL014819

Roche, O., Gilbertson, M. A., Phillips, J. C., & Sparks, S. S. (2004). Experimental study of gas-fluidized granular flows with implications for pyroclastic flow emplacement. *Journal of Geophysical Research: Solid Earth*, *109*. doi: 10.1029/2003JB002916

Rowley, P. J., Roche, O., Druitt, T. H., & Cas, R. (2014). Experimental study of dense pyroclastic density currents using sustained, gas-fluidized granular flows. *Bulletin of Volcanology*, *76*, 1-13. doi: 10.1007/s00445-014-0855-1

Scharff, L., Hort, M., & Varley, N. R. (2019). First in-situ observation of a moving natural pyroclastic density current using doppler radar. *Scientific Reports*, *9*. doi: 10.1038/s41598-019-43620-w

Schiesser, W. E. (2012). *The numerical method of lines: integration of partial differential equations*. Elsevier.

Schneider, C. A., Rasband, W. S., & Eliceiri, K. W. (2012). Nih image to imagej: 25 years of image analysis. *Nature Methods*, *9*. doi: 10.1038/nmeth.2089

Scott, A. C., & Glasspool, I. J. (2005). Charcoal reflectance as a proxy for the emplacement temperature of pyroclastic flow deposits. *Geology*, *33*(7), 589–592. doi: 10.1130/G21474.1

Scott, G. D., & Kilgour, D. M. (1969). The density of random close packing of spheres. *Journal of Physics D: Applied Physics*, *2*. doi: 10.1088/0022-3727/2/6/311

Shampine, L. F., & Reichelt, M. W. (1997). The matlab ode suite. *SIAM journal on scientific computing*, *18*(1), 1–22.

Sparks, R. S., Barclay, J., Calder, E. S., Herd, R. A., Komorowski, J. C., Luckett, R., . . . Woods, A. W. (2002). Generation of a debris avalanche and violent pyroclastic density current on 26 december (boxing day) 1997 at soufrière hills volcano, montserrat. *Geological Society Memoir*, *21*. doi: 10.1144/GSL.MEM.2002.021.01.18

Sparks, R. S. J. (1976). Grain size variations in ignimbrites and implications for the transport of pyroclastic flows. *Sedimentology*, *23*(2), 147–188. doi: 10.1111/J.1365-3091.1976.TB00045.X

Stinton, A. J., Cole, P. D., Stewart, R. C., Odbert, H. M., & Smith, P. (2014). The 11 February 2010 partial dome collapse at Soufrière Hills Volcano, Montserrat. *Geological Society, London, Memoirs*, *39*(1), 133–152. doi: 10.1144/M39.7

Stroberg, T. W., Manga, M., & Dufek, J. (2010). Heat transfer coefficients of natural volcanic clasts. *Journal of Volcanology and Geothermal Research*, *194*(4), 214–219. doi: 10.1016/J.JVOLGEORES.2010.05.007

Sulpizio, R., Dellino, P., Doronzo, D. M., & Sarocchi, D. (2014). Pyroclastic density currents: State of the art and perspectives. *Journal of Volcanology and Geothermal Research*, *283*, 36–65. doi: 10.1016/J.JVOLGEORES.2014.06.014

Thouret, J. C. (1990). Effects of the november 13, 1985 eruption on the snow pack and ice cap of nevado del ruiz volcano, colombia. *Journal of Volcanology and Geothermal Research*, *41*. doi: 10.1016/0377-0273(90)90088-W

Thouret, J. C., Ramírez, J., Gibert-Malengreau, B., Vargas, C. A., Naranjo, J. L., Vandemeulebrouck, J., . . . Funk, M. (2007). Volcano-glacier interactions on composite cones and lahar generation: Nevado del Ruiz, Colombia, case study. *Annals of Glaciology*, *45*, 115-127. doi: 10.3189/172756407782282589

Vale, A. B., Jenkins, L. T., Phillips, J. C., Rust, A. C., Hogg, A. J., Kilgour, G., & Seward, A. (2023). *Dataset and software: Heat transfer in pyroclastic density current - ice interactions: Insights from experimental and numerical simulations.* doi: 10.5281/zenodo.8278922

Vollmer, M. (2009). Newton's law of cooling revisited. *European Journal of Physics*, *30*(5), 1063.

Walder, J. (2000a). Pyroclast/snow interactions and thermally driven slurry formation. Part 1: Theory for monodisperse grain beds. *Bulletin of Volcanology*, *62*, 105-118.

Walder, J. (2000b). Pyroclast/snow interactions and thermally driven slurry formation. Part 2: Experiments and theoretical extension to polydisperse tephra. *Bulletin of Volcanology*, *62*, 119-129.

Walding, N., Williams, R., Rowley, P., & Dowey, N. J. (2023). Cohesional behaviours in volcanic material and the implications for deposit architecture. *Pre-print submitted to: Bulletin of Volcanology*. doi: 10.31223/X5WM2F

Waythomas, C. (2014). Water, ice and mud: lahars and lahar hazards at ice- and snow-clad volcanoes. *Geology Today*, *30*(1), 34–39. doi: 10.1111/gto.12035

Wilson, C. J. N. (1980). The role of fluidization in the emplacement of pyroclastic claws: An experimental approach. *Journal of Volcanology and Geothermal Research*, *8*(2-4), 231–249. doi: 10.1016/0377-0273(80)90106-7

Yamamoto, T., Takarada, S., & Suto, S. (1993). Pyroclastic flows from the 1991 eruption of unzen volcano, japan. *Bulletin of Volcanology*, *55*. doi: 10.1007/BF00301514